IOPscience iopscience.iop.org

Home Search Collections Journals About Contact us My IOPscience

The spin-gap state and the phase transition in the δ-phase $Tl_xV_2O_5$ polaronic bronze

This article has been downloaded from IOPscience. Please scroll down to see the full text article.

2002 J. Phys.: Condens. Matter 14 5045

(http://iopscience.iop.org/0953-8984/14/19/325)

View the table of contents for this issue, or go to the journal homepage for more

Download details:
IP Address: 171.66.16.104
The article was downloaded on 18/05/2010 at 06:40

Please note that terms and conditions apply.

INSTITUTE OF PHYSICS PUBLISHING JOURNAL OF PHYSICS: CONDENSED MATTER

J. Phys.: Condens. Matter **14** (2002) 5045–5059 PII: S0953-8984(02)32951-5

The spin-gap state and the phase transition in the δ-phase $Tl_xV_2O_5$ polaronic bronze

Masashige Onoda and Junichi Hasegawa

Institute of Physics, University of Tsukuba, Tennodai, Tsukuba 305-8571, Japan

Received 23 January 2002, in final form 5 April 2002
Published 2 May 2002
Online at stacks.iop.org/JPhysCM/14/5045

Abstract

The crystal structure and electronic properties of δ-phase bronze $Tl_xV_2O_5$, where $0.47 \leqslant x \leqslant 0.496$, have been explored by means of x-ray four-circle diffraction and through measurements of lattice constants, electrical resistivity, thermoelectric power, magnetization, and electron paramagnetic resonance. The structure of $Tl_{0.479}V_2O_5$ redetermined with residual factors of $R = 0.052$ and $R_w = 0.041$ indicates that the trellis-layer model is applicable to this system as in the case of δ-$Ag_{2/3}V_2O_5$ in the low-temperature phase. A spin-gap behaviour derived from that model and the hopping conduction of negative small polarons are found. A phase transition takes place at around 150 K accompanied by significant changes of the superexchange coupling constants (or spin-gap energies) and the carrier-creation energies.

M This article features online multimedia enhancements

1. Introduction

Many transition-metal oxides and ternary oxide bronzes with unfilled d bands have been investigated intensively in order to understand the properties of correlated-electron, electron–phonon-coupling, and quantum spin-fluctuation systems. A search for novel phenomena and functions has also been performed.

Various low-dimensional spin networks exist in the vanadium oxide system. For example, in a half-filled insulator system CaV_nO_{2n+1} with $n = 2$–4 that consists of V_nO_{2n+1} layers formed by sharing edges and corners of VO_5 pyramids and Ca atoms situated between the layers [1–3], two-dimensional $S = \frac{1}{2}$ networks are formed at the V^{4+} site of the $\frac{1}{n+1}$-depleted square lattice. Here, for $n = 2$ and 4, there appear spin-gap states essentially originating from corner-sharing dimerization [3, 4] and from weakly coupled metaplaquettes [5, 6], respectively. On the other hand, for $n = 3$, a stripe-phase magnetic ordering takes place [7], and its microscopic origin has recently been revealed in detail [8]. The quarter-filled insulator NaV_2O_5, which has a structure similar to that of CaV_2O_5 [3, 9–11], shows one-dimensional $S = \frac{1}{2}$ magnetic properties with spins attached to a V–O–V molecular orbital [9, 12] and undergoes a transition to the spin-gap

state at $T_c = 34$ K with a lattice distortion [13]. The crossover between the spin-gap and the linear-chain properties as a function of band filling through the $Ca_{1-x}Na_xV_2O_5$ system [14] was explored in order to clarify whether it is continuous or not.

Recently, the structural and electronic properties of the δ-phase vanadium bronze $Ag_xV_2O_5$, where $0.65 \leqslant x \leqslant 0.90$, have been investigated from multiple viewpoints [15]. In this system, the band filling can be varied substantially. The structure redetermined for $x = 0.68$ indicates that two crystallographically independent V ions in the V_2O_5 double layers have valences close to the average value expected from the chemical formula. This system is characterized against the composition as follows. For the range $0.65 \leqslant x \leqslant 0.75$, first-order phase transitions with structural, transport, and magnetic anomalies appear at $T_{c1} \simeq 220$ K. Below this temperature, together with significant reduction of the superexchange coupling constants, a nearly $\frac{1}{6}$-filled compound has a spin gap derived from the trellis-layer model [16], the application of which is justified from consideration of superexchange couplings, while other compositions probably remain paramagnetic. For $0.80 \leqslant x < 0.85$, the only transport anomaly occurs at $T_{c2} \simeq 170$ K, and for $0.85 \leqslant x \leqslant 0.90$ no anomaly exists there. The magnetic properties for $0.80 \leqslant x \leqslant 0.90$ essentially exhibit linear-chain behaviours with the V–O–V molecular orbital. Thus, in the crossover region between the spin-gap state and the linear-chain state, the paramagnetic phases without long-range order are stable down to low temperatures, notwithstanding the existence of antiferromagnetic couplings.

This work is focused on $Tl_xV_2O_5$ with $x \approx 0.50$. There has been previous work as regards the crystal structure and electronic properties of this system [17]. It indicates that this compound belongs to the group of δ-phase vanadium bronzes, as stated above, and the Tl concentration ranges from 0.44 to 0.48, which is significantly smaller than the lower limit ($x = 0.65$) in $Ag_xV_2O_5$ [15]. The electrons donated by Tl are postulated to be localized preferentially on one side of two V sites. In this case, $Tl_{0.50}V_2O_5$ has a quarter-filled band. While the Ag ions in $Ag_{0.68}V_2O_5$ at room temperature are situated at disordered two sites, the Tl ions have a single site. So, for $x = 0.50$, the Tl sites are completely occupied. A phase transition to a spin-glass-like state at $T_c \simeq 160$ K is also suggested. Thus, δ-$Tl_xV_2O_5$ appears to show properties different from those of the Ag-based system. With the aim of clarifying the origin and details of the structural and electronic properties, the present work was planned. Section 2 describes the crystal structure redetermined by means of single-crystal x-ray diffraction, and in section 3 the electronic properties revealed through measurements of electrical resistivity, thermoelectric power, magnetization, and electron paramagnetic resonance (EPR) are discussed. Section 4 is devoted to further discussion and conclusions.

2. Crystal structure

2.1. Sample preparation, chemical analysis, and lattice constants

Sintered specimens of $Tl_xV_2O_5$ with the nominal range $0.44 \leqslant x \leqslant 0.50$ were prepared by the solid-state reaction method as follows. Appropriate mixtures of V_2O_5 (99.99% purity), V_2O_3, and Tl_2O_3 (99.9% purity) for $x \neq 0.5$ and Tl_2O (99.9% purity) for $x = 0.5$ were ground and pressed into pellets, where V_2O_3 was made according to the procedure described in [18]. These were sealed in quartz tubes and then heated at 853 K for 24 h. The preparation of single crystals with the nominal composition $Tl_{0.50}V_2O_5$ was also carried out by the Bridgman method at 882 or 953 K using the above mixtures. For the prepared specimens, an x-ray powder diffraction analysis and an electron-probe microanalysis (EPMA) were performed at room temperature using a Rigaku RAD-IIC diffractometer with Cu Kα radiation and a JEOL JXA-8621, respectively.

Table 1. The composition dependences of the lattice constants of δ-$Tl_xV_2O_5$ at room temperature. For $x = 0.479$, results determined by means of the single-crystal diffraction are indicated.

x	a (Å)	b (Å)	c (Å)	β (deg)	V (Å^3)
0.47	11.598(1)	3.6831(5)	9.6269(9)	100.83(1)	403.91(8)
0.475(5)	11.599(2)	3.6843(9)	9.629(1)	100.88(2)	404.1(1)
0.479(2)	11.5980(8)	3.6840(6)	9.6293(5)	100.826(5)	404.11(6)
0.481(10)	11.592(1)	3.6835(4)	9.616(1)	100.86(1)	403.24(7)

For the sintered specimens with the nominal compositions of $0.47 \leqslant x \leqslant 0.50$, the x-ray powder diffraction patterns indicated a single phase, while for those with $0.44 \leqslant x \leqslant 0.46$, small amounts of impurity phases appeared. On the basis of the EPMA, the Tl concentrations for $x = 0.48$ and 0.50 were estimated to be 0.481(10) and 0.475(5), respectively. The single crystals extracted from the sintered specimens were small fragile platelets. The crystalline specimen obtained by the Bridgman method was a lump of platelet and the x-ray diffraction pattern showed significant amounts of impurity phases, TlV_3O_8 and β-phase $Tl_xV_2O_5$. The EPMA result indicated that these impure compounds are present between the platelets, so single-phase platelets could be cut off. For these platelets, the Tl concentration was estimated to be 0.496(10). In the following, we shall use the nominal composition for $x = 0.47$ and the EPMA ones for other specimens. As presented in section 3, for the sintered specimens with $x = 0.475$, all of the transport and magnetic measurements were performed; for those with $x = 0.47$ and 0.481, all of the measurements except the EPR ones were made; and for the single-phase platelets with $x = 0.496$, the transport properties alone were measured. The composition region for the single phase revealed here is shifted upward, $0.47 \leqslant x \leqslant 0.496$, as compared with the previous result [17].

Table 1 shows the composition dependence of the lattice constants at room temperature, obtained from the comparison with the powder diffraction pattern calculated on the basis of the atomic parameters of $Tl_{0.479}V_2O_5$ which will be described in section 2.2. The results determined by an x-ray four-circle diffraction are also listed. The lattice constants change little with x. For the single-phase platelets, the diffraction peak positions with respect to $\boldsymbol{c}^*$, in which the direction is perpendicular to the cleavage plane, are consistent with the parameters listed in table 1. The temperature dependence of the lattice constants for $x = 0.481$ in the heating process is shown in figures 1(a)–(e). There is no abrupt change of the lattice constants. With decreasing temperature, the lattice constants a, c, and β decrease monotonically, while the b-axis constant shows the inverse tendency. The resultant decrease of the volume V is attributable to the shrinking of the atomic displacement caused by thermal vibrations.

2.2. *Structure determination*

The x-ray four-circle diffraction measurements were carried out on a Rigaku AFC-7R diffractometer (custom-made) and a DI-XRD CAD4 with graphite-monochromated Mo Kα radiation at 297 K. The single crystal with dimensions of $0.10 \times 0.06 \times 0.01$ mm made by the solid-state reaction method with the nominal composition $Tl_{0.50}V_2O_5$ was mounted on a glass fibre. The intensity data were collected over a maximum 2θ range of 90° using the ω–2θ scan technique. Of 1837 unique reflections, 1057 reflections with $|F_o| \geqslant 3\sigma$, F_o and σ being an observed structure factor and its standard deviation, respectively, were used. Lorentz polarization, the absorption correction, and the secondary extinction correction were applied, where the transmission factors were in the range 0.47–1. The internal consistency of the reflections was estimated on the basis of F_o^2 to be $R_{int} = 0.080$.

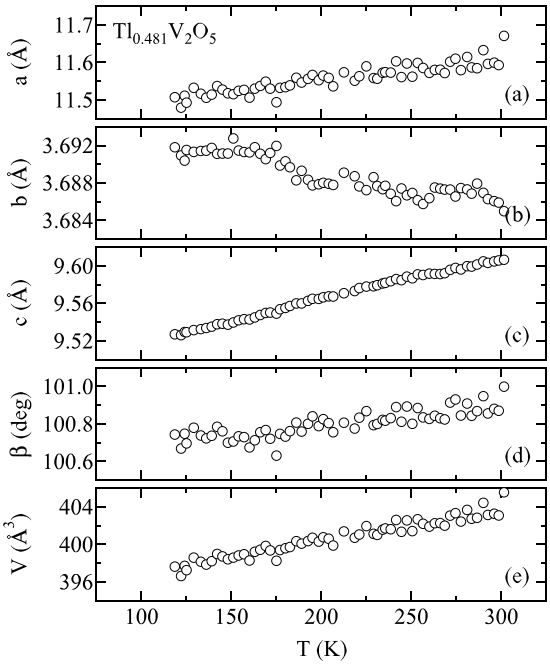

Figure 1. The temperature dependences of the lattice constants of δ-$Tl_{0.481}V_2O_5$ in the heating process.

Through the systematic absences of reflections, a statistical analysis of the intensity distribution, and the successful refinement of the structure, the crystal data were determined to be: monoclinic with space group $C2/m$ (No 12); $Z = 4$; μ(Mo Kα)= 23.501 mm^{-1}; and $D_{\mathrm{cal}} = 4.598$ Mg m^{-3}. The lattice constants are already listed, in table 1.

The Patterson map was successfully explained on the basis of the previous atomic parameters [17]. Therefore, the present structure was refined using the parameters for Tl and V atoms as initial values by full-matrix least-squares calculations with anisotropic displacement parameters. The atomic scattering factors were taken from [19], and anomalous dispersion effects were included with the values given by [20]. The residual factors defined as

$$R = \left[\sum(|F_{\mathrm{o}}| - |F_{\mathrm{c}}|)^2\right] \Big/ \left(\sum |F_{\mathrm{o}}|\right) \tag{1}$$

and

$$R_{\mathrm{w}} = \left\{\left[\sum w(|F_{\mathrm{o}}| - |F_{\mathrm{c}}|)^2\right] \Big/ \left(\sum w F_{\mathrm{o}}^2\right)\right\}^{1/2} \tag{2}$$

where $|F_{\mathrm{c}}|$ is a calculated structure factor, are finally[1] $R = 0.052$ and $R_{\mathrm{w}} = 0.041$. All of the calculations were performed using the teXsan crystallographic software package [21].

The atomic coordinates, equivalent isotropic thermal parameters, and anisotropic displacement parameters are listed in table 2. Selected interatomic distances are listed in table 3. The atomic coordinates refined here are roughly consistent with the previous results [17], but significant deviations of 1×10^{-2} exist for oxygen atoms O1 and O5. Thus, the interatomic distances for these atoms are different from those presented previously. Moreover, standard

[1] Supplementary data files are available from the article's abstract page in the online journal; see http://www.iop.org.

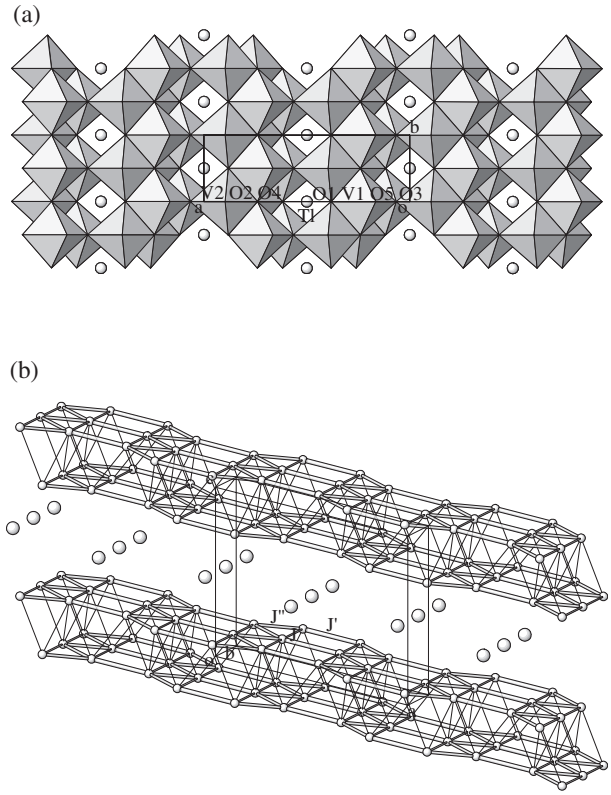

Figure 2. The crystal structures of δ-$Tl_{0.479}V_2O_5$ at 297 K: (a) the projection on the ab-plane using the polyhedral scheme and (b) a clinographic view of the network of Tl (large spheres) and V (small spheres) ions, where the thick lines and the thin lines denote the V–V paths at similar and dissimilar z-levels, respectively; J and J' indicate the corner-sharing paths for the significant exchange couplings; and J'' shows the edge-sharing one.

deviations in this work are greatly improved. Figure 2(a) shows the crystal structure projected on the ab-plane using the polyhedral scheme and figure 2(b) shows a clinographic view of the network of Tl and V ions. There exist two independent vanadium atoms labelled V1 and V2. The V1–O and V2–O bond lengths range from 1.599 to 2.549 and 1.616 to 2.359 Å, respectively, indicating that each V atom forms a distorted octahedron. The short bonds of 1.599 and 1.616 Å correspond to the double bond V=O. The structure is described in terms of the $V1O_6$ and $V2O_6$ octahedra which are joined by sharing edges and corners to form double layers of V_2O_5.

The effective valences at the V1 and V2 sites are estimated to be 4.64 and 4.70, respectively, on the basis of the bond-length–bond-strength relation [22]. Thus, the valence distribution of V ions is approximately homogeneous, which contrasts strikingly with the previous conclusion that the electrons are localized at one side of the V sites [17][2]. The ground-state wavefunctions for the $V1O_6$ and $V2O_6$ octahedra are expressed by $0.953d_{xy} - 0.304d_{yz}$ and $0.970d_{xy} + 0.244d_{yz}$, respectively, where $\boldsymbol{x} \parallel \boldsymbol{a}$ and $\boldsymbol{y} \parallel \boldsymbol{b}$, with the use of the Hartree–Fock function for V^{4+} [23]. The effective valences of the oxygen atoms at the O1–O5 sites are given as 1.97, 1.73, 1.95, 1.88, and 1.82, respectively. Due to the V=O bond, the hole densities at the O2 and O5 sites are significantly large.

[2] The bond-length–bond-strength relation with the previous atomic parameters leads to the conclusion that the electrons are localized at the V2 site.

Table 2. Atomic coordinates, equivalent isotropic thermal parameters B_{eq} (Å^2), and anisotropic displacement parameters U_{ij} of δ-$Tl_{0.479}V_2O_5$ at 297 K, where $y = 0$ and $U_{12} = U_{23} = 0$ for all of the atoms. B_{eq} and U_{ij} are defined by $B_{eq} = \frac{8}{3}\pi^2[U_{11}(aa^*)^2 + U_{22}(bb^*)^2 + U_{33}(cc^*)^2 + 2U_{12}aa^*bb^* \cos\gamma + 2U_{13}aa^*cc^* \cos\beta + 2U_{23}bb^*cc^* \cos\alpha]$, and the parameters are defined in the thermal factor form $T = \exp[-2\pi^2(a^{*2}U_{11}h^2 + b^{*2}U_{22}k^2 + c^{*2}U_{33}l^2 + 2a^*b^*U_{12}hk + 2a^*c^*U_{13}hl + 2b^*c^*U_{23}kl)]$. The occupancy probability for Tl is 0.958(4).

Atom	x	z	B_{eq}	U_{11}	U_{22}	U_{33}	U_{13}
Tl	$\frac{1}{2}$	$\frac{1}{2}$	2.44(2)	0.0419(5)	0.0250(4)	0.0250(4)	0.0038(3)
V1	0.2073(1)	0.8439(2)	0.71(2)	0.0071(5)	0.0066(5)	0.0130(7)	0.0011(5)
V2	0.0911(1)	0.1550(2)	0.68(2)	0.0086(6)	0.0065(6)	0.0112(7)	0.0030(5)
O1	0.3820(5)	0.8726(7)	0.9(1)	0.006(2)	0.009(2)	0.018(3)	0.003(2)
O2	0.1031(6)	0.3249(7)	1.3(1)	0.017(3)	0.026(4)	0.008(3)	0.004(2)
O3	0.0659(5)	0.9061(7)	0.8(1)	0.002(2)	0.010(3)	0.018(3)	0.002(2)
O4	0.2599(5)	0.1131(7)	0.9(1)	0.008(2)	0.005(2)	0.024(4)	0.007(2)
O5	0.1646(6)	0.6760(7)	1.3(1)	0.015(3)	0.023(4)	0.009(3)	0.001(2)

Table 3. Selected interatomic distances (Å) and angles (deg) of δ-$Tl_{0.479}V_2O_5$ at 297 K, where the translation codes are (i) x, y, z; (ii) $\frac{1}{2} - x, -\frac{1}{2} - y, 1 - z$; (iii) $\frac{1}{2} - x, \frac{1}{2} - y, 1 - z$; (iv) $x, -y, 1 + z$; (v) $x, y, -1 + z$; (vi) $-x, -y, 1 - z$; (vii) $\frac{1}{2} + x, \frac{1}{2} + y, z$; (viii) $\frac{1}{2} + x, -\frac{1}{2} + y, z$; (ix) $\frac{1}{2} - x, -\frac{1}{2} - y, 2 - z$; (x) $\frac{1}{2} - x, \frac{1}{2} - y, 2 - z$; (xi) $-x, -y, -z$.

$V1O_6$ polyhedra		Tl(i)–O5(ii, iii, vii, viii)	2.949(5)
V1(i)–O1(i)	1.993(6)	V–V distances	
V1(i)–O3(i)	1.850(5)	V1(i)–V1(ix, x)	3.507(3)
V1(i)–O4(ii, iii)	1.911(2)	V2(i)–V2(xi)	3.317(3)
V1(i)–O4(iv)	2.549(7)	V1(i)–V2(iii)	2.974(2)
V1(i)–O5(i)	1.599(7)	V1(i)–V2(iv)	3.508(2)
$V2O_6$ polyhedra		V1(i)–V2(vi)	3.464(2)
V2(i)–O2(ii, iii)	1.895(2)	V–O–V angles	
V2(i)–O2(i)	1.616(7)	V1(ii)–O4(i)–V1(iii)	149.2(4)
V2(i)–O3(v)	2.359(7)	V2(ii)–O1(i)–V2(iii)	152.8(4)
V2(i)–O3(vi)	1.805(6)	V1(i)–O3(i)–V2(vi)	142.8(4)
V2(i)–O4(i)	2.071(6)	V1(i)–O1(i)–V2(ii, iii)	99.8(2)
TlO_8 polyhedra		V1(ii)–O4(i)–V2(i)	96.6(2)
Tl(i)–O2(ii, iii, vii, viii)	2.902(5)		

The Tl atoms are slightly deficient, with the occupancy probability 0.958(4). This probability leads to the chemical formula of $Tl_{0.479(2)}V_2O_5$, which agrees with the EPMA result $Tl_{0.475(5)}V_2O_5$. The Tl atoms are located between the V_2O_5 layers and surrounded with eight O atoms. The Tl–O bond lengths range from 2.902 to 2.949 Å, so their average value is 2.926 Å, leading to the ionic radius 1.546 Å, which agrees well with that for eight coordinations of the Tl^+ ion [24]. The thermal parameter for Tl is significantly larger than those for V and O atoms, which may be attributed to the Tl vacancy.

3. Electronic properties

3.1. Electrical resistivity

The electrical resistivities for the sintered specimens, ρ_s, and for the direction perpendicular to the c^*-axis of the platelets, $\rho_{\perp c^*}$, of $Tl_xV_2O_5$ were measured by a dc method in the temperature region between 100 and 300 K. For ρ_s and $\rho_{\perp c^*}$, four- and two-terminal methods were used, respectively.

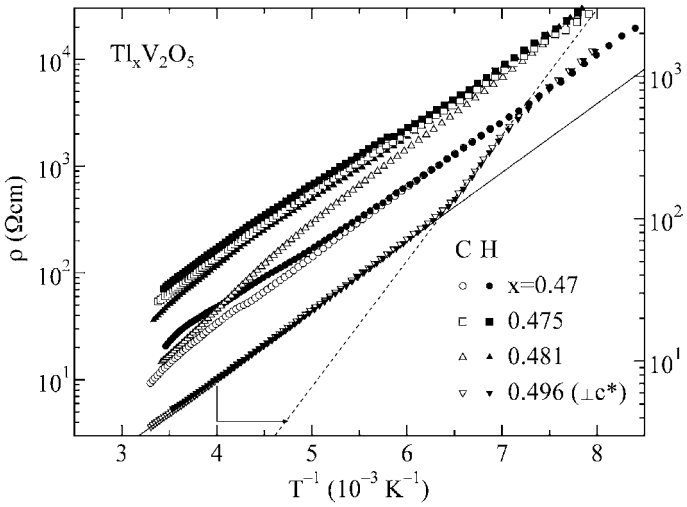

Figure 3. The temperature dependences of the electrical resistivities for the sintered specimens, ρ_s, and for the platelets, $\rho_{\perp c^*}$, of δ-$Tl_xV_2O_5$ in the cooling 'C' and heating 'H' processes, where the full and dotted lines show fits to equation (3) with parameters for $T > T_{c\rho}$ and $T < T_{c\rho}$ listed in table 4, respectively.

Table 4. The composition dependence of the parameters in equations (3) and (4), E_ρ (K), S_0 (μV K^{-1}), and E_S (K), of δ-$Tl_xV_2O_5$. For $x = 0.496$, results for the direction perpendicular to the c^*-axis are indicated.

	$T > T_{c\rho}, T_{cS}$			$T < T_{c\rho}, T_{cS}$		
x	E_ρ	S_0	E_S	E_ρ	S_0	E_S
0.47	—	−61(1)	146(4)	—	518(36)	1121(48)
0.475(5)	—	−43.1(3)	72(1)	—	456(19)	899(26)
0.481(10)	—	−52.0(5)	152(1)	—	682(8)	1342(11)
0.496(10)	1113(1)	−27.4(3)	94(1)	2034(9)	639(23)	1243(37)

The resistivities ρ_s and $\rho_{\perp c^*}$ as a function of the inverse temperature are shown in figure 3. Here, the open and full symbols indicate results for the cooling and heating processes, respectively. All of the specimens basically exhibit semiconducting conductions and the mobilities at room temperature are in the range of 10^{-4}–10^{-5} cm^2 V^{-1} s^{-1} for the carrier density 5×10^{21} cm^{-3}, suggesting a small-polaron conduction. The temperature dependence of ρ_s slightly deviates from the straight line. For $x = 0.47$ and 0.481, thermal hysteresis is significant and sample dependent. These results may be partly attributed to granular texture effects of the specimens, considering the results for the platelets as described below. So they are not discussed here. On the other hand, the temperature dependence of $\rho_{\perp c^*}$ is characterized by two lines. From the full line and the dotted one in figure 3, the energy gaps E_ρ defined by

$$\rho_{\perp c^*} = \rho_0 \exp(E_\rho/T) \tag{3}$$

where ρ_0 is assumed to be a constant, are estimated as listed in table 4. The gap estimated at low temperatures is about twice as large as that at high temperatures. The change of E_ρ takes place at $T_{c\rho} \simeq 158$ K without thermal hysteresis.

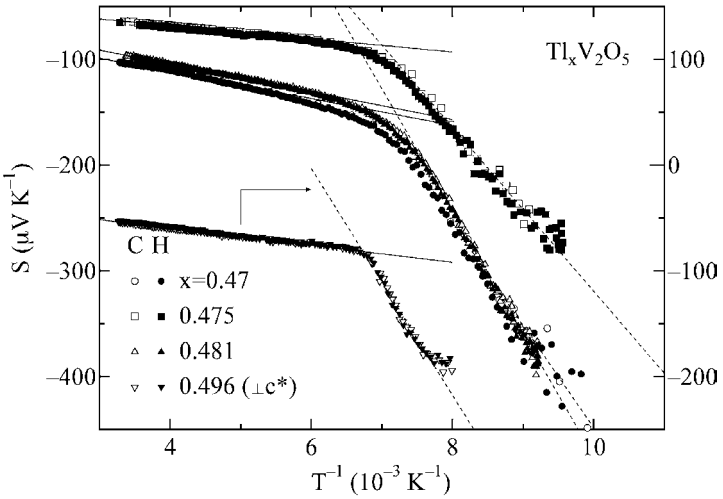

Figure 4. The temperature dependences of the thermoelectric powers for the sintered specimens, S_s, and for the platelets, $S_{\perp c^*}$, of δ-$Tl_xV_2O_5$ in the cooling 'C' and heating 'H' processes, where the full and dotted lines indicate fits to equation (4) with the parameters for $T > T_{cS}$ and $T < T_{cS}$ listed in table 4, respectively.

3.2. Thermoelectric power

The dc measurements of thermoelectric powers for the sintered specimens, S_s, and for the direction perpendicular to the c^*-axis of the platelets, $S_{\perp c^*}$, of $Tl_xV_2O_5$ were performed at temperatures between 100 and 300 K.

Figure 4 shows the thermoelectric power data against the inverse temperature, where the open and full symbols indicate results for the cooling and heating processes, respectively. All of the data exhibit semiconducting behaviours, which is consistent with the resistivity result. They are negative, suggesting electron carrier conduction. The result for $x = 0.475$ appears to be a bit different from those for other compositions. This may be partly attributed to the possible oxygen vacancy as will be pointed out in section 3.3. As described in section 2.1, only this specimen was prepared with Tl_2O, so the oxygen concentration is expected to be slightly different from those for other compositions prepared with Tl_2O_3. Taking account of the difference in oxygen concentrations, the specimen with $x = 0.475$ is considered to be possessed of more electrons, leading to the smaller $|S|$. In other words, the composition dependence of S_s may be regarded as being small for the specimens with the same oxygen deficiency. The temperature dependences of S_s and $S_{\perp c^*}$ are qualitatively similar, since granular texture effects of the specimens are less significant for the thermoelectric power. Their magnitudes are considered to be different due to the anisotropic conduction based on the layered structure. A comparison between S_s and $S_{\perp c^*}$ suggests that the absolute value for the direction parallel to the c^*-axis is smaller than $S_{\perp c^*}$. For S_s and $S_{\perp c^*}$, there exist anomalies without thermal hysteresis at $T_{cS} \simeq 145$ and 150 K, respectively, accompanied with the rapid change of the temperature variations. Here, T_{cS} for $S_{\perp c^*}$ is roughly consistent with $T_{c\rho}$ for $\rho_{\perp c^*}$. On the basis of the full lines for $T > T_{cS}$ and the dotted ones for $T < T_{cS}$ in figure 4, the temperature-independent value S_0 and the gap E_S, empirically defined by

$$S = -eE_S/T + S_0, \tag{4}$$

are estimated as listed in table 4. The gap obtained at low temperatures has increased by about 10^3 K as compared with that at high temperatures. The significant difference between E_ρ

Table 5. The susceptibility parameters of δ-$Tl_xV_2O_5$, where C is the Curie constant (emu K (mol V)$^{-1}$); J, J', and J'' are the exchange constants (K); Δ is the spin-gap energy (K); C_{isolate} and $T_{\text{W}}^{\text{isolate}}$ are the Curie constant and the Weiss temperature (K) for the impurity spin; and χ_0 is the constant susceptibility (10^{-5} emu (mol V)$^{-1}$). The upper and lower rows for each composition indicate results for the temperature regions above and below $T_{c\chi}$, respectively, where C, C_{isolate}, $T_{\text{W}}^{\text{isolate}}$, and χ_0 are assumed not to vary at $T_{c\chi}$.

x	C	J	J'	J''	Δ	C_{isolate}	$T_{\text{W}}^{\text{isolate}}$	χ_0
0.47	0.091(2)	56(17)	638(4)	244(24)	562	0.00187(2)	3.5(1)	2.40(4)
	0.091	134(3)	540(3)	274(12)	387	0.00187	3.5	2.40
0.475(5)	0.100(3)	81(22)	616(6)	276(27)	511	0.00240(3)	4.6(1)	2.41(5)
	0.100	151(1)	521(2)	325(4)	355	0.00240	4.6	2.41
0.481(10)	0.094(1)	76(7)	599(2)	254(9)	501	0.00129(1)	3.71(7)	1.96(2)
	0.094	149(1)	529(1)	331(2)	364	0.00129	3.71	1.96

and E_S may be characteristic of small-polaron motion if a variable-range hopping mechanism does not work. This can be understood by considering the narrow tails of localized states which extend into the forbidden gap and a band of compensated levels originating from the Tl doping near the middle of the gap. Thus, E_S in equation (4) corresponds to the width between the energies at the Fermi level and at the tail edge, and E_ρ in equation (3) is the sum of the energies for carrier creation and for hopping. As found in table 4, the increase of E_S with decreasing temperature is roughly equal to that of E_ρ. Thus, the transport anomalies in $Tl_xV_2O_5$ are characterized not by the change of hopping energies but by that of carrier-creation energies.

In the high-temperature limit where all of the mobile charge carriers are created and the fraction of V sites occupied by them is fixed, S_0 corresponds to the Heikes formula [25]:

$$S_{\text{p}} = \frac{k}{e} \ln\left(\frac{x}{2-x}\right) \tag{5}$$

where k is the Boltzmann coefficient. This formula leads to $S_{\text{p}} = -94\ \mu\text{V K}^{-1}$ for $x = 0.50$, which qualitatively accounts for S_0 for $T > T_{cS}$. In order to estimate the hopping energy of the polaron precisely, a small temperature dependence of the pre-exponential term ρ_0 in equation (3), which is proportional to T and $T^{3/2}$ for adiabatic and nonadiabatic polarons, respectively, should be considered. However, this is difficult, since the high-temperature measurement region is not wide. On the other hand, S_0 estimated from the low-temperature data is positive, so another scattering mechanism should be added.

3.3. Magnetization

The magnetizations of the sintered specimens of $Tl_xV_2O_5$ were measured by the Faraday method with a field of up to 1 T. Here, the temperature region was limited to between 4.2 and 550 K, since measurements at the higher temperatures gave rise to thermally irreversible magnetization results, possibly due to a phase transition [17]. Both cooling and heating processes were examined. The magnetic susceptibility χ was deduced from the linear part of the magnetization–field (M–H) curve with a decreasing field.

Figure 5(a) shows the χ-data as a function of temperature. For all of the compositions, the temperature dependences are considered to be similar and they are reversible for the cooling and heating processes in the measurement region. There exists a rounded maximum at about 360 K, as expected for low-dimensional spin systems. Below 80 K, a Curie-like tail appears, which may come from the phase such as a lattice imperfection or a magnetic impurity that cannot

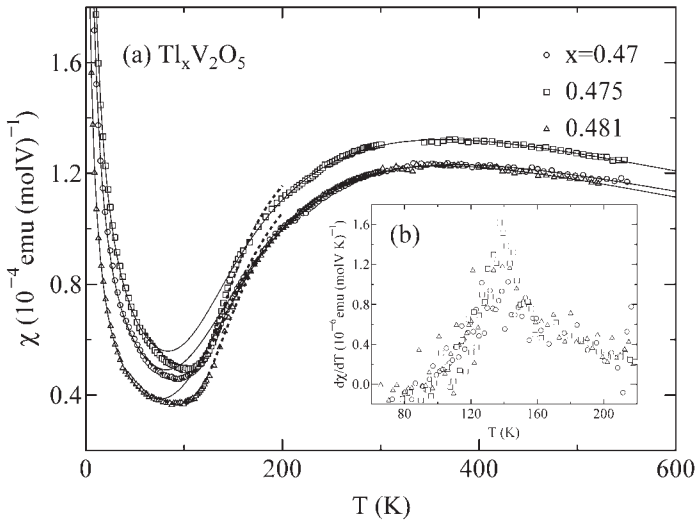

Figure 5. The temperature dependences of (a) the magnetic susceptibility χ and (b) its temperature derivative $d\chi/dT$ for δ-$Tl_xV_2O_5$ in the heating process, where the full and dotted curves in (a) are drawn on the basis of equation (6) with parameters for $T > T_{c\chi}$ and $T < T_{c\chi}$ listed in table 5, respectively.

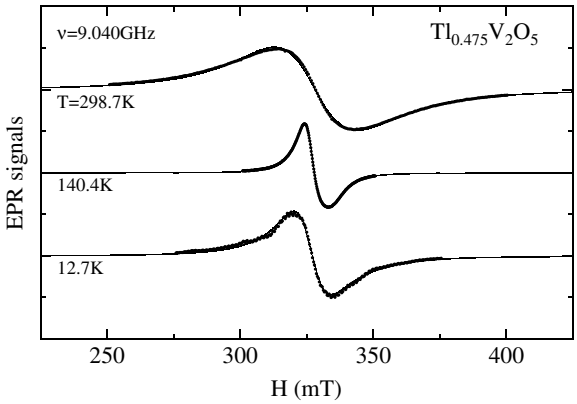

Figure 6. EPR signals of δ-$Tl_{0.475}V_2O_5$ at 12.7, 140.4, and 298.7 K, where the dots and the full curves represent the experimental and calculated results, respectively.

be detected by standard x-ray powder diffraction techniques. Thus, the intrinsic behaviour of χ exhibits a spin gap having a significant decrease of the susceptibility with decreasing temperature. In addition, the temperature dependence of χ appears to change at $T_{c\chi} \simeq 145$ K, below which χ decreases more rapidly with decreasing temperature. As shown in figure 5(b), the temperature derivative of χ has a peak at about 140 K.

As described in section 2.2, the ground-state wavefunctions at the V1 and V2 sites in $Tl_{0.479}V_2O_5$ are both of d_{xy} type, so the superexchange couplings through the oxygen p orbitals between the V ions at a similar z-level in the ab-plane are expected to be most effective. Thus, the simplified spin network, the so-called trellis-layer model, is applicable to this system, as shown in figure 2(b), where the thick lines and the thin lines denote the V–V paths at similar

and dissimilar z-levels, respectively; J and J' denote two kinds of corner-sharing V–V path, and J'' is the edge-sharing one[3]. The susceptibility is thus described in the form

$$\chi = \frac{4C}{J_{\max}}\chi^* + \chi_{\text{isolate}} + \chi_0 \tag{6}$$

$$\chi_{\text{isolate}} = \frac{C_{\text{isolate}}}{T + T_{\text{W}}^{\text{isolate}}} \tag{7}$$

where χ^* is the reduced fit function calculated by quantum Monte Carlo simulations for the trellis-layer model [16]; C is the Curie constant; $J_{\max}$ is the largest exchange constant in the system; χ_{isolate} is the Curie–Weiss-type susceptibility of the isolated V^{4+} ions with parameters C_{isolate} and the Weiss temperature $T_{\text{W}}^{\text{isolate}}$; and χ_0 corresponds to the temperature-independent susceptibility of the Van Vleck orbital and diamagnetic components. The full curves in figure 5(a) are drawn on the basis of the parameters listed in table 5. The spin gaps Δ estimated from these superexchange coupling constants are also listed. Except for the temperature region between 70 and $T_{c\chi}$, the agreement between the experimental and calculated results is satisfactory. Since the V^{4+} ions have the average g-factor of 1.963, as will be described in section 3.4, the Curie constants listed here agree roughly with the values expected from a model where Tl doping x gives rise to an unpaired electron with $\frac{x}{2}$ per V ion, $C = 0.181x$. For $x = 0.475$, C is a little larger than the value expected from the results for other compositions. This suggests that at this composition, the effect of oxygen vacancies is relatively large. Taking the chemical formula as $Tl_xV_2O_{5-\delta}$, δ is estimated to be 0.016, 0.039, and 0.020 for $x = 0.47$, 0.475, and 0.481, respectively. In order to confirm this result, precise thermogravimetric analysis is needed. Possible weak couplings between the trellis layers should also be examined.

At around $T_{c\chi}$, the structural anomaly is not significant, as shown in figures 1(a)–(e). Therefore, the spin network considered above may be still valid. A deviation from the calculated curve is expected to be attributable to modification of the superexchange coupling constants with the assumption that C, C_{isolate}, $T_{\text{W}}^{\text{isolate}}$, and χ_0 do not change. In effect, the temperature dependence of χ below $T_{c\chi}$ is explained as shown in figure 5(a) by the dotted curves with the parameters listed in table 5. For all of the compositions, the relation $J' > J'' > J$ is still valid, and J below $T_{c\chi}$ is twice as large as that above $T_{c\chi}$.

3.4. Electron paramagnetic resonance

EPR measurements for the sintered specimen of $Tl_{0.475}V_2O_5$ were performed in a heating process at temperatures between 12 and 300 K at 9.04 GHz using a JEOL JES-TE200 spectrometer. The spectra were asymmetric and the spin susceptibility extracted on the basis of the integration of the signal, taking account of the temperature dependence of a Q-factor, agrees well with the magnitude of $\chi - \chi_0$ in equation (6). Examples of the spectra at 298.7, 140.4, and 12.7 K are shown in figure 6. They are explained as shown by the full curves on the assumption that the g-factor and the peak-to-peak linewidth W with the shape of a Lorentzian have uniaxial angular dependences with respective principal values $g_{Z\,(XY)}$ and $W_{Z\,(XY)}$ parallel (perpendicular) to the principal axis $\boldsymbol{Z}$. Here, $g_{XY} = 1.981$ and $g_Z = 1.927$ in the temperature region performed, leading to the space-averaged g-factor $\langle g \rangle = 1.963$. This result corresponds to an average of the g-tensors at V1 and V2 sites, and it is basically consistent with the d_{xy}-type ground state as discussed in [14]. Taking account of the result of the crystal-field analysis, it is found that the $\boldsymbol{X}$- or $\boldsymbol{Y}$-axis corresponds to the twofold $\boldsymbol{b}$-axis, and the $\boldsymbol{Z}$-axis is located in the ac-plane.

[3] The Heisenberg Hamiltonian is defined as $H = \sum_{\langle i,j \rangle} J\boldsymbol{S}_i \cdot \boldsymbol{S}_j$, $\boldsymbol{S}_i$ being the spin operator at site i.

Figure 7(a) shows the temperature dependences of W_{XY} and W_Z. They decrease monotonically with decreasing temperature at temperatures above $T_{cW} \simeq 140$ K, while below T_{cW}, a rapid upturn occurs. T_{cW} nearly corresponds to T_{cS} and $T_{c\chi}$ as presented before. For $T > T_{cW}$, the anisotropy of the linewidth appears to be small, but for $T < T_{cW}$, it increases significantly with decreasing temperature. Generally, the EPR linewidth is a measure of the relaxation rate for spin fluctuations perpendicular to the spin dynamics, although its analysis is complicated by the effect of the field on the spin dynamics. For insulating spin systems, there exist several kinds of typical relaxation mechanism, on the basis of the dipole–dipole (dd) interaction, the anisotropic exchange (ae) interaction, and the Dzyaloshinsky–Moriya (DM) antisymmetric exchange interaction [14]. Considering that the spins are distributed homogeneously with a population p $(=x/2)$ and assuming that the correlation time τ_c is given by $2\hbar/J_{\mathrm{eff}}$, $\hbar$ and J_{eff} being Planck's constant and an effective exchange constant, respectively, the space-averaged linewidth due to the dd interaction is given by

$$\langle W_{\mathrm{dd}} \rangle = 2\sqrt{3} p g^3 \mu_{\mathrm{B}}^3 J_{\mathrm{eff}}^{-1} \sum_{i>j} r_{ij}^{-6} \tag{8}$$

where μ_{B} is the Bohr magneton and r_{ij} is the distance between spins. It is estimated to be $\langle W_{\mathrm{dd}} \rangle = 0.6$ mT for the case of $x = 0.475$ and $J_{\mathrm{eff}} = J'$. The width due to the ae interaction expressed as

$$\langle W_{\mathrm{ae}} \rangle = 2^{-1}\sqrt{3}\, \Delta g^4\, g^{-5} \mu_{\mathrm{B}}^{-1} J_{\mathrm{eff}}, \tag{9}$$

where $\Delta g = 2.0023 - g$, leads to $\langle W_{\mathrm{ae}} \rangle = 0.06$ mT. These are much smaller than the observed values. On the other hand, the width due to the DM interaction, $\boldsymbol{d}_{ij} \cdot (\boldsymbol{S}_i \times \boldsymbol{S}_j)$, with the vector $\boldsymbol{d}_{ij}$ defined between $\boldsymbol{S}_i$ and $\boldsymbol{S}_j$, is given by

$$\langle W_{\mathrm{DM}} \rangle = 9^{-1}\sqrt{3}\, \Delta g^2\, g^{-3} \mu_{\mathrm{B}}^{-1} J_{\mathrm{eff}} \tag{10}$$

in the high-temperature limit, where $|\boldsymbol{d}| = 2^{-1}\, \Delta g\, g^{-1} J_{\mathrm{eff}}$. It is noted that none of the midpoints of the V–V paths responsible for J, J', and J'' in the trellis-layer model considered here are inversion centres (where J' and J'' are the constants of superexchange between the crystallographically inequivalent V sites). Equation (10) provides $\langle W_{\mathrm{DM}} \rangle = 35$ mT, which is comparable to the experimental result. The approximately uniaxial dependence of W and the anisotropy of $W_Z > W_{XY}$ with the $\boldsymbol{Z}$-axis located in the ac-plane are easily explained if, for example, $\boldsymbol{d}_{ij} \parallel \boldsymbol{Z}$. In order to determine the precise direction of $\boldsymbol{d}_{ij}$, measurements for the single-crystal specimens are necessary.

At temperatures below T_{cW}, where the carrier-creation energy and the spin-gap energy change significantly as listed in tables 4 and 5, another or an additional relaxation mechanism should be considered, since the temperature dependence is quite different from the high-temperature behaviour, and the anisotropy of the linewidth defined as $W_{\mathrm{an}} = (W_Z - W_{XY})/2$ (figure 7(b)) at the lowest temperature may be too large to be understood in terms of the mechanisms described above. Assuming that the increase in the linewidth at low temperatures corresponds to a certain kind of critical slowing down of the spins due to antiferromagnetic correlation, this contribution is empirically expressed as

$$W - W_\infty \propto (T - T^*)^{-1} \tag{11}$$

where W_∞ is the limiting value at high temperatures, and T^* is the critical temperature [4, 26]. The data below 100 K are described qualitatively by this relation as indicated by the full curve in figure 7(b), where $W_\infty = 3.9(1)$ mT and $T^* = 5(1)$ K. This suggests that an antiferromagnetically correlated state exists at temperatures much smaller than the spin-gap energy, notwithstanding that the intrinsic spin system exhibits a gap.

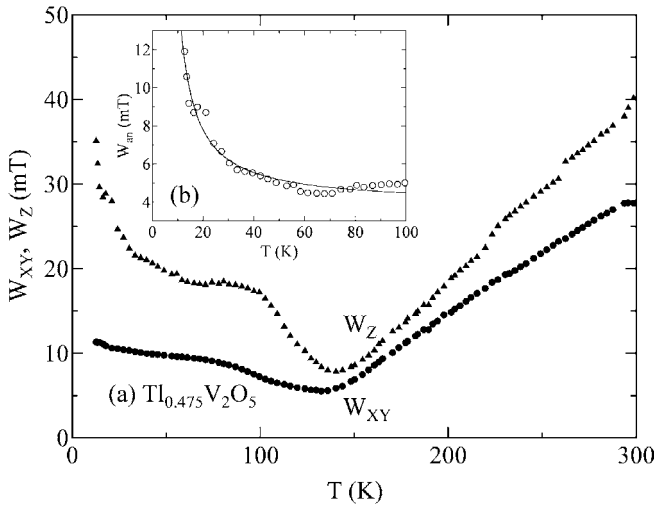

Figure 7. The temperature dependences of (a) the EPR linewidths W_{XY} and W_Z, and (b) W_{an} for δ-$Tl_{0.475}V_2O_5$ in the heating process. The full curve in (b) indicates a fit to equation (11).

Another possible explanation for the low-temperature behaviour of the linewidth is a modulation of the hyperfine interaction A_{hf} by the local electron hopping with a frequency ν_h. Here, it is stressed that the spectra observed at temperatures much smaller than the spin-gap energy are mainly originating from the impurity spin with a concentration 2%, estimated from the susceptibility analysis. On the assumption that this spin is isolated due to the lattice imperfection (possibly due to the Tl vacancy) in the $Tl_{0.475}V_2O_5$ phase, it is possible to derive information, except for the exchange effects, as was done for the slightly oxygen-deficient $Ag_2V_4O_{11}$ insertion electrode [27]. Here, the hopping frequency is expected to be larger than A_{hf} at the lowest temperature, since hyperfine spectra are not resolved. The temperature dependence of ν_h may correspond to that of W_{an}. Assuming an exponential temperature dependence for ν_h:

$$\nu_h \propto \exp(-\Delta_h/T), \tag{12}$$

the excitation energy for the hopping process, Δ_h, at temperatures below 50 K is estimated to be 13.9(7) K with a result almost identical to the full curve shown in figure 7(b). This extremely small value may be responsible for the local electron hopping between localized states under the electrostatic field of the Tl or oxygen vacancies, which is not related to the temperature dependence of the resistivity at high temperatures.

In order to reach a definite conclusion for the EPR relaxation at temperatures below T_{cW}, further considerations are needed.

4. Further discussion and conclusions

The structural and electronic properties of the δ-phase $Tl_xV_2O_5$ system with the single-phase region $0.47 \leqslant x \leqslant 0.496$ have been investigated from multiple viewpoints. In this composition range, the structural and electronic properties are similar to each other, taking account of oxygen concentrations.

On the basis of the crystal structure of $Tl_{0.479}V_2O_5$ redetermined in this work, two crystallographically independent V ions in the V_2O_5 double layers are found to have valences

close to the average value expected from the chemical formula. The crystal-field analysis indicates that the superexchange coupling between the V ions at a similar z-level is most effective, so the trellis-layer model may be applied to this system as in the case of δ-$Ag_{2/3}V_2O_5$ in the low-temperature phase.

All of the compositions exhibit the hopping conduction of negative small polarons with significant difference between E_ρ and E_S, and they have spin-singlet properties as expected from the trellis-layer model, where spins are attached to a single V ion; and J' ($\approx$600 K) $> J'' > J$. The phase transition takes place at about 150 K with significant changes of the superexchange coupling constants (spin-gap energies) and the carrier-creation energies. This may be related to the structural modification, possibly due to the ordering of deficient Tl ions and/or the electron–phonon coupling, although the change of powder diffraction pattern at low temperatures is not significant. The spin dynamics is also discussed in the framework of usual EPR relaxation mechanisms: at high temperatures, the antisymmetric exchange interaction is dominant, while at low temperatures, considerations based on the antiferromagnetic correlation and the hopping motion for isolated electrons are presented.

In δ-$Ag_xV_2O_5$ with $0.65 \leqslant x \leqslant 0.90$, the composition $x = \frac{2}{3}$ alone ($\frac{1}{6}$ filling) has the spin-gapped state in the low-temperature phase below the structural and electronic transition temperature. It is found that the nearly $\frac{1}{8}$-filled $Tl_xV_2O_5$ without site randomness is already in a singlet state at temperatures above room temperature. Therefore, the V_2O_5 layer of $Ag_{2/3}V_2O_5$ below the transition temperature is considered to be close to that of $Tl_xV_2O_5$.

The size of J' in $Tl_xV_2O_5$ seems to be rather large in spite of the small filling. The superexchange couplings J_{pd} may depend both on the hopping integral t for transfer between the $3d_{xy}$ orbital of vanadium and the $2p_y$ orbital of oxygen and on the V–O–V angle ϕ [4, 8, 12]. Considering that t is proportional to $D^{-7/2}$, where D is the V–O distance, J_{pd} is expected to be linear in $D^{-14}\cos^4\phi$ [28]. For the half-filled insulator CaV_2O_5 with corner-sharing dimerization, it is known that $J' \simeq 660$ K, $D = 1.905$ Å, and $\phi = 132.9°$ [3]. These values lead to $J' \simeq 140$ K for $Tl_{0.50}V_2O_5$ with structural parameters given in section 2, which is about 1/4 of the value listed in table 5. This discrepancy can be reconciled by considering that J' in CaV_2O_5 is the exchange coupling between the symmetry-related V ions, while that in $Tl_xV_2O_5$ is the exchange coupling between the crystallographically inequivalent V sites.

In conclusion, notwithstanding rather complicated structures of the δ-phase vanadium bronze, the electronic properties have been explained qualitatively with a simple model, since the VO_6 polyhedra in the Tl- and Ag-based compounds have the singlet ground-state d_{xy} orbital. In order to understand the relationship between the structure and the phonon-coupled electronic properties in detail, further investigations are necessary.

References

[1] Bouloux J-C and Galy J 1973 *Acta Crystallogr.* B **29** 1335
[2] Bouloux J-C and Galy J 1973 *Acta Crystallogr.* B **29** 269
[3] Onoda M and Nishiguchi N 1996 *J. Solid State Chem.* **127** 359
[4] Onoda M and Ohyama A 1998 *J. Phys.: Condens. Matter* **10** 1229
[5] Kodama K *et al* 1997 *J. Phys. Soc. Japan* **66** 793 and references therein
[6] Fukumoto Y and Oguchi A 1998 *J. Phys. Soc. Japan* **67** 2205 and references therein
[7] Harashina H, Kodama K, Shamoto S, Taniguchi S, Nishikawa T, Sato M, Kakurai K and Nishi M 1996 *J. Phys. Soc. Japan* **65** 1570
[8] Nishiguchi N, Onoda M and Kubo K 2001 unpublished
[9] Smolinski H, Gros C, Weber W, Peuchert U, Roth G, Weiden M and Geibel C 1998 *Phys. Rev. Lett.* **80** 5164
[10] Meetsma A, de Boer J L, Damascelli A and Palstra T T M 1998 *Acta Crystallogr.* C **54** 1558

[11] von Schnering H G, Grin Y, Kaupp M, Somer M, Kremer R K, Jepsen O, Chatterji T and Weiden M 1998 *Z. Kristallogr.—New Cryst. Struct.* **213** 246
[12] Horsch P and Mack F 1998 *Eur. Phys. J.* B **5** 367
[13] Isobe M and Ueda Y 1996 *J. Phys. Soc. Japan* **65** 1178
[14] Onoda M and Kagami T 1999 *J. Phys.: Condens. Matter* **11** 3475
[15] Onoda M and Arai R 2001 *J. Phys.: Condens. Matter* **13** 10399
[16] Johnston D C *et al* 2000 *Preprint* cond-mat/0001147
[17] Ganne M, Jouanneaux A, Tournoux M and Le Bail A 1992 *J. Solid State Chem.* **97** 186
[18] Onoda M, Ohta H and Nagasawa H 1991 *Solid State Commun.* **79** 281
[19] Cromer D T and Waber J T 1974 *International Tables for X-Ray Crystallography* vol 4, ed J A Ibers and W C Hamilton (Birmingham: Kynoch) section 2
[20] Creagh D C and McAuley W J 1992 *International Tables for Crystallography* vol C, ed A J C Wilson (Boston, MA: Kluwer)
[21] teXsan 1992 *Crystal Structure Analysis Package* (The Woodlands, TX: Molecular Structure Corporation)
[22] Zachariasen W H 1978 *J. Less-Common Met.* **62** 1
[23] Freeman A J and Watson R E 1965 *Magnetism* part A, vol 2, ed G T Rado and H Suhl (New York: Academic)
[24] Shannon R D 1976 *Acta Crystallogr.* A **32** 751
[25] Heikes R R 1961 *Thermoelectricity* ed R R Heikes and R W Ure (New York: Interscience)
[26] Huber D L 1972 *Phys. Rev.* B **6** 3180
[27] Onoda M and Kanbe K 2001 *J. Phys.: Condens. Matter* **13** 6675
[28] Harrison W A 1980 *Electronic Structure and the Properties of Solids* (San Francisco, CA: Freeman)